Energy Engineering

Tech Science Press

https://doi.org/10.32604/ee.2026.080456

ARTICLE

Transient Thermodynamic, Sensitivity and Multi-Objective Design Analysis of a Multilayer PCM-Assisted Evacuated Tube Solar Collector

Dheyaa Abdulraheem Khalaf[1,*] and Ammar Sami Mohammad[2]

[1]Fuel and Energy Techniques Engineering Department, Technical Engineering College–Baghdad, Middle Technical University (MTU), Baghdad, Iraq

[2]Mechanical Power Technical Engineering Department, Al-Amarah University College, Maysan, Iraq

*Corresponding Author: Dheyaa Abdulraheem Khalaf. Email: dheyaaabdkhalaf@mtu.edu.iq

Received: 10 February 2026; Accepted: 30 April 2026; Published: 18 June 2026

Highlights

- A transient enthalpy-based lumped model is developed for a multilayer PCM–assisted ETSC under time-dependent irradiance.
- PCM integration reduces peak temperatures vs. a no-PCM reference by 0.284 K (HTF) and 0.416 K (absorber) for the reported baseline.
- Solar thermal and exergy efficiencies show different transient behavior; $\overline{\eta}_{solar} = 0.8788$ while $\overline{\psi}_{solar} = 0.0098$.
- Time-step refinement (0.2 → 0.1 s) preserves $\overline{\eta}_{solar}$ and lowers RMS energy-balance residual.
- NSGA-II optimization quantifies the thermal–exergy trade-off and provides reproducible representative Pareto designs.

ABSTRACT: Transient thermodynamic analysis of a multilayer phase-change material (PCM)–assisted evacuated tube solar collector (PCM–ETSC) is presented. A compact enthalpy-based numerical model is formulated to capture coupled heat transfer among the absorber tube, a mixed-mean heat-transfer fluid (HTF) control volume, and multiple PCM layers with staggered melting temperatures under time-dependent irradiance. Performance is evaluated using solar-referenced thermal and exergy efficiencies and reported over a sunlit window defined by $G(t) > 0.1\,G_{max}$. For the baseline run, the simulated temperature ranges are $T_f \in [298.000, 306.489]$ and $T_t \in [298.000, 310.432]$ K with PCM, compared with $T_f \in [298.000, 306.774]$ and $T_t \in [298.000, 310.848]$ K without PCM, corresponding to reductions in peak HTF and absorber temperatures of 0.284 and 0.416 K, respectively. The sunlit-window means are $\overline{\eta}_{solar} = 0.8788$ (87.88%) and $\overline{\psi}_{solar} = 0.0098$ (0.98%), while the maximum instantaneous solar exergy efficiency reaches 0.0133. A time-step refinement from $\Delta t = 0.2$ to 0.1 s leaves $\overline{\eta}_{solar}$ unchanged to six decimal places (0.878817 vs. 0.878816) and reduces the RMS global energy-balance residual from 0.086164 to 0.048758 J per step, supporting numerical consistency. Multilayer phase change is evidenced by layer-resolved liquid-fraction histories; using $f_l \geq 0.99$ as a completion metric, none of the three PCM layers reach completion within the 6 h horizon for the reported baseline (peak temperatures remain below the threshold implied by $T_{m,k}$ and the mushy band). One-at-a-time sensitivity studies quantify the influence of HTF mass flow rate, uniform PCM thickness, and a common melting-temperature shift. Multi-objective optimization using NSGA-II (MATLAB gamultiobj) maps the trade-off between $\overline{\eta}_{solar} \in [0.780, 0.908]$ and $\overline{\psi}_{solar} \in [0.007, 0.018]$, with representative thermal-oriented, exergy-oriented, and compromise designs reported explicitly. The results show that first-law and second-law metrics diverge under transient charging and that multilayer PCM integration can buffer peak temperatures while enabling design trade-offs between delivered heat quantity and quality.

KEYWORDS: Phase change material; evacuated tube solar collector; transient analysis; exergy analysis; sensitivity analysis; multi-objective optimization; NSGA-II

1 Introduction

1.1 Solar Thermal Systems, Emissions, and the Rationale for Storage

Solar thermal technologies convert incident solar radiation into heat that can be delivered to buildings and light industrial processes at temperatures that are often sufficient without a high-pressure steam infrastructure. When solar heat displaces electric resistance heating or direct fossil combustion for domestic hot water and for low-temperature process heat, fuel use and local combustion-related pollutant emissions are avoided at the point of application; where the marginal electricity mix is carbon-intensive, the substitution can also reduce greenhouse gas emissions associated with electricity use [1,2]. The more practical limitation is the temporal mismatch between solar supply and instantaneous heat demand: diurnal irradiance cycles and short transients can cause collector output to fluctuate unless a buffering mechanism is present. Distributed thermal energy storage integrated at, or near, the collector can smooth outlet swings and extend the time period over which useful heat is delivered compared with purely instantaneous collection [3,4].

1.2 Evacuated Tube Collectors and Integration of PCM

Evacuated tube solar collectors (ETSCs) are designed to minimize convective heat losses from the absorber (the heat collecting surface) by enclosing it in a glass tube that incorporates an evacuated annulus, while transferring the absorbed solar gain to an internal fluid path; commercial designs typically use a U tube or similar routing depending on the configuration of the finished product [5]. Compared to many non-evacuated glazed collectors of similar aperture, ETSCs can retain good thermal performance at moderate operating temperatures, which is important for domestic hot-water systems and other similar applications where heat loss mechanisms and stagnation behavior affect annual yield [5,6].

Phase change materials (PCMs) are capable of storing thermal energy by absorbing and later releasing latent heat across a limited range of transition temperatures, giving them a greater volumetric storage density compared to sensible storage alone [7]. When the PCM is located next to the absorber region of an ETSC, this leads to an alternative pathway for latent charging/discharging, which changes the transient temperature response of the collector when compared to an otherwise identical collector without PCM [8]. Scheme 1 illustrates the modelled domain used in this work (glass envelope/vacuum annulus, absorber tube, HTF path, PCM layers, and ambient heat loss passing through).

1.3 Literature on PCM–ETSC Systems and Multilayer PCM Concepts

PCM-assisted evacuated-tube collectors have been investigated under a variety of internal configurations (heat pipe vs. direct flow), PCM placements and encapsulation strategies, and operating conditions. This variety makes direct, point by point matching of a single temperature curve an unfair standard unless the geometry, boundary conditions, and measurement definitions are closely matched. At the same time, there are qualitative behaviours reported in literature that a defensible transient model should reproduce under comparable irradiance and flow regimes: latent buffering affects temperature–time histories, melting dynamics reflect both flow and heat transfer pathways, and first law and second law indicators may evolve differently during transient operation.

On the experimental/field side, Wu et al. [9] demonstrated collector-side energy behaviour for PCM-integrated ETSCs under outdoor conditions and highlighted the impact of storage on transient thermal

delivery. ALali et al. [10] provided a with/without PCM comparison for a U pipe ETSC and thereby allotted a basic comparison point for the effect of PCM on the evolution of charging temperature. Pathak et al. [11] emphasize that energetic and exegetic measures do not necessarily trend in tandem over time windows motivating the parallel reporting of thermal and exergy indicators as opposed to just relying on one as a proxy for the other, Uniyal et al. [12] studied melting/heat transfer behaviour in a U tube configuration, shedding light on the progress of liquid fraction and the time scales over which partial vs. near complete melting occurred. From the performance metrics perspective.

Complementary—PCM based solar water heating systems and enhancements to evacuated tubes reviews cover similar design themes, and point notably toward a continuing lack of reporting transient, consistently internally defined second laws [13–15].

In this context, multilayer (multi-Tm) PCM concepts can extend the latent operating band in a feasible manner, by spreading latent uptake through a larger temperature range and suppressing premature saturation associated to a single melting plateau [16]. Since staged melting is an inherently coupled transient evolution of absorber temperature, HTF extraction, interfacial heat transfer and ambient losses, steady-state or heavily simplified formulations can yield an erroneous layer activation order, a false partial melting progression and inaccurate energy/exergy performance across realistic irradiance windows. Accordingly, the present formulation adopts a Petela-based solar exergy input definition [17], an enthalpy-consistent fixed-grid mushy-zone treatment for phase change [18], NSGA-II for multi-objective search [19], and a standard validation/uncertainty reference to frame the benchmarking and diagnostics [20].

More recent work expands the design space beyond purely PCM, single geometry implementations. Optimization and parametric design studies have been reported for U type evacuated tube collectors with PCM [21], while other studies offered methods to correlate HTF flow-rate choice to performance indicators and transient temperatures [22]. Cascaded/cascaded like PCM layouts have been leveraged to increase the effective temperature span of the stored heat, while assisting with saturation behavior [23], while nano enhanced PCM techniques offer some variation to the effective storage and transfer behavior [24].

In parallel, system level studies and reviews state that fairly comparing PCM–ETSC isn't straightforward due to practical constraints (low (<50%) conductivities, contact resistances, and geometry dependent losses) as well as definition dependent KPIs and inconsistent reporting practices for transients [25–27]. A collection of component level enhancement strategies—including combined optical/thermal loss reduction approaches [28], finned/lobed storage geometries and advanced working fluids [29], tests combining U tube PCM integration with observability [30], conductive augmentation (wire meshes) [31], and optimization of PCM–tube structures/geometry [32]—serve to further reinforce that both the hardware chosen, and the value of the chosen metric notably influence the final performance output.

1.4 Novelty Relative to Steady-State and Single-Layer PCM Studies

The present work does not replace the fundamental collector balances; it retains an absorber–HTF–PCM representation consistent with ETSC studies cited above and focuses on two distinctions that are central to the reviewers' concerns. First, relative to steady or quasi-steady post-processing, a transient enthalpy-based PCM formulation is needed to capture the ordering of melting events across layers and early-time second-law trends associated with rapid temperature excursions. Second, relative to single-layer PCM, multilayer staging spreads latent effects across multiple melting bands and, under sustained charging, delays saturation behavior compared with concentrating latent uptake in one plateau [16].

1.5 Objectives and Contributions

The objectives are: (1) to document a transient enthalpy-based model for a multilayer PCM-assisted ETSC with explicit boundary and initial conditions and a stated mushy-region regularization; (2) to validate the model using PCM–ETSC literature benchmarks at the level of transient trends supported by published experiments, complemented by a global energy-balance diagnostic; (3) to quantify thermal and exergy performance under time-dependent irradiance, including transient exergy behavior; (4) to conduct one-at-a-time sensitivity analysis for mass flow rate, PCM thickness, and PCM melting temperature; and (5) to perform NSGA-II-based multi-objective optimization between thermal and exergy efficiencies and to interpret representative Pareto points for different design priorities.

The contributions are summarized as follows: (i) a transient modeling framework for multilayer PCM around an ETSC absorber that preserves the baseline governing physics of the collector model; (ii) analysis of staged melting and its implications for saturation timing relative to a no-PCM baseline under the same boundary conditions; (iii) joint reporting of thermal and exergy efficiencies under transient charging; (iv) sensitivity results that separate parameters influencing instantaneous efficiency from parameters influencing storage duration; and (v) a Pareto-based design map from NSGA-II showing thermal–exergy trade-offs without altering the underlying physical model.

Broader contribution to the energy sector and sustainability context. The practical value of PCM-assisted ETSC configurations extends beyond documenting transient temperature histories. The core value of these systems is their ability to buffer the erratic spikes and drops in heat delivery. This stabilizes solar energy for low-to-medium temperature needs—sectors that usually fall back on fossil fuels the moment the sun dips. Instead of just modeling, we use a transient screening framework that pairs numerical diagnostics with Pareto-based mapping to guide actual design choices. We specifically focus on three things: cutting down thermal stress from stagnation, stretching out the hours of useful operation, and making sure fossil-fuel displacement in domestic heating is consistent rather than hit-or-miss. Perhaps the most critical takeaway here is the tension between heat quantity and quality. As our study shows, optimizing for thermal efficiency doesn't automatically mean you've optimized for exergy, and forgetting that distinction is where most collector-to-load matching fails.

2 Methodology

2.1 System Description and Modeling Assumptions

In this work, we present the mathematical model of a PCM-assisted evacuated tube solar collector (PCM–ETSC) and investigate its response during a charging transient. Solar radiation is absorbed at the tube absorber and is partitioned into (i) useful heat transfer to the heat-transfer fluid (HTF), (ii) heat exchange with surrounding PCM layers, and (iii) thermal loss to the ambient. The PCM is arranged as multiple annular layers around the absorber, each assigned a melting temperature to promote staged melting. The model adopts standard simplifications used in transient collector-scale analysis: (i) the absorber tube and the HTF are treated as lumped (mixed-mean) control volumes; (ii) each PCM layer is represented by one layer-mean temperature and liquid fraction; (iii) effective heat-transfer coefficients represent absorber–HTF and absorber–PCM coupling; and (iv) irradiance is prescribed as a smooth time-dependent profile. The intent is to produce a transparent transient model suitable for sensitivity analysis and multi-objective design mapping, while stating limitations explicitly (Section 4).

Rationale for using a lumped (mixed-mean) model. A lumped model is selected because the objective of this work is design screening under transient forcing (sensitivity and Pareto mapping), where robustness and reproducibility across many parametric runs are more valuable than resolving local gradients that

are not measured in the available benchmarks. In the present context, several quantities of interest—sunlit-window means $\overline{\eta}_{solar}$ and $\overline{\psi}_{solar}$, peak temperatures, and layer-mean liquid fractions—are naturally expressed at a control-volume level and can be computed consistently without introducing additional spatial degrees of freedom that would require extra boundary data. The main trade-off is that intra-tube and intra-layer temperature nonuniformity is represented implicitly through effective parameters (notably h_{tf} and h_{PCM}). This limitation is stated explicitly and is partly addressed by reporting numerical diagnostics and by benchmarking trend-level behavior against published PCM–ETSC studies (Sections 2.4 and 2.5).

Fig. 1 provides the schematic used throughout this paper to define the modeled domain (glass envelope/vacuum annulus, absorber tube, HTF path, multiple PCM layers, and the heat-loss path to ambient).

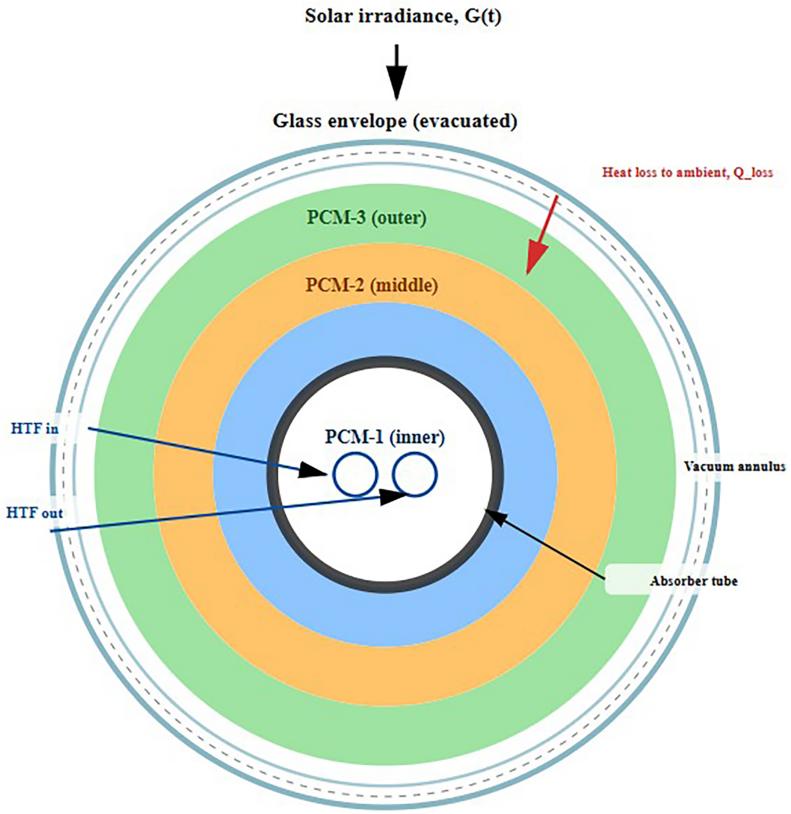

Figure 1: Schematic of the multilayer PCM-assisted evacuated tube solar collector (PCM–ETSC) considered in the lumped transient model, showing the prescribed solar irradiance G(t), the evacuated glass envelope and vacuum annulus, the absorber tube and HTF flow path, the PCM layers (from inner to outer), and the ambient heat-loss term Q_loss.

2.2 Governing Equations

All temperatures are reported in kelvin (K), and heat-transfer rates are reported in watts (W). The aperture (reference) area is denoted by Ac (m^2). Parameter provenance (effective coefficients). In Eqs. (1)–(5), the coefficients h_{tf}, h_{PCM}, and η_{opt} are treated as effective, collector-scale parameters within the lumped formulation. Accordingly, they represent the combined influence of multiple unresolved resistances including internal convection, contact and conduction paths, and optical/absorptive effects—rather than being assigned to separate physical layers in the model. To keep the manuscript fully faithful to the

reported results, the numerical values used are exactly those in the archived MATLAB implementation that generated Section 3.5 ($h_{tf} = 150\,Wm^{-2}K^{-1}, h_{PCM} = 50\,Wm^{-2}K^{-1},$ and $\eta_{opt} = 0.73$).

2.2.1 Absorbed Solar Input

$$Q_{solar}(t) = \max(\eta_{opt} A_c G(t), 0) \tag{1}$$

2.2.2 Absorber Tube (Lumped Energy Balance)

$$m_t c_t \frac{dT_t}{dt} = Q_{solar} - Q_{t\to f} - Q_{t\to PCM} - Q_{loss} \tag{2}$$

$$Q_{t\to f,raw} = h_{tf} A_c (T_t - T_f), Q_{t\to f} = \max(Q_{t\to f,raw}, 0) \tag{3}$$

$$Q_{t\to PCM} = \sum_k h_{PCM} A_c (T_t - T_{PCM,k}) \tag{4}$$

$$Q_{loss} = \max(0, \sigma A_c (T_t{}^4 - T_{amb}{}^4)) \tag{5}$$

2.2.3 Heat-Transfer Fluid (HTF; Mixed-Mean Control Volume)

$$m_f c_f \frac{dT_f}{dt} = Q_{t\to f} - \dot{m}_f c_f (T_f - T_{in}) \tag{6}$$

In the baseline simulations, the inlet temperature is prescribed as $T_{in} = T_{amb}$

2.2.4 PCM Layers (Enthalpy Method with Mushy-Zone Regularization)

Each PCM layer k is represented by a layer-mean temperature $T_{pcm,k}$ and a liquid fraction $f_l \in [0, 1]$. Phase change is handled by an enthalpy-consistent mushy-zone regularization in which the liquid fraction is a linear function of temperature over a finite melting interval of width ΔT_{mushy} [18]. In the reported simulations, $\Delta T_{mushy} = 6$ K (i.e., $T_{m,k} \pm 3$ K).

$$f_k(T_{PCM,k}) = \min\left(1, max\left(\frac{T_{PCM,k} - (T_{m,k} - \Delta T_{mushy}/2)}{\Delta T_{mushy}}\right)\right) \tag{7}$$

$$c_{p,eff,k} = c_{p,k} + \frac{L_{lat,k}}{\Delta T_{mushy}} \text{ (within mushy interval)}, \text{ and } c_{p,eff,k} = c_{p,k} \text{ otherwise} \tag{8}$$

$$m_{PCM,k} c_{p,eff,k} \frac{dT_{PCM,k}}{dt} = h_{PCM} A_c (T_t - T_{PCM,k}) \tag{9}$$

2.2.5 Performance Indicators (Thermal and Exergy)

$$\eta_{solar}(t) = \min\left(\frac{Q_{t\to f}}{Q_{solar}}, 1\right) \text{ for } Q_{solar} > 0; \eta_{solar}(t) = 0 \text{ otherwise} \tag{10}$$

$$\psi_{sun} = 1 - \frac{4}{3}\frac{T_{amb}}{T_{sun}} + \frac{1}{3}\left(\frac{T_{amb}}{T_{sun}}\right)^4, \dot{E}_{x,in} = Q_{solar}\psi_{sun} \text{ [17]} \tag{11}$$

$$\dot{E}_{x,out,raw} = \dot{m}_f c_f \left[(T_f - T_{amb}) - T_{amb} \ln\left(\frac{\max(T_f, T_{amb})}{T_{amb}}\right)\right] \tag{12}$$

$$\psi_{solar}(t) = \frac{\dot{E}_{x,out,raw}}{\dot{E}_{x,in}} \text{ for } \dot{E}_{x,in} > 0; \psi_{solar}(t) = 0 \text{ otherwise} \tag{13}$$

Windowed (sunlit-mean) KPIs are denoted by an $\overline{\eta}_{solar}$ and $\overline{\psi}_{solar}$ are the sunlit-window mean values of $\eta_{solar}(t)$ and $\psi_{solar}(t)$, respectively, evaluated over the mask $G(t) > 0.1\, G_{max}$.

2.3 Numerical Solution Procedure and Prescribed Irradiance

The governing equations are advanced using an explicit forward-Euler scheme. The baseline figures and time histories use $\Delta t = 0.2$ s on a 6 h horizon ($t_{end} = 6 \times 3600$ s). A refined run uses $\Delta t = 0.1$ s for the time-step check. For multi-objective optimization, $\Delta t = 1$ s is employed to reduce objective-evaluation cost. The incident irradiance is prescribed as:

$$G(t) = G_{max} \exp\left(-\left(\frac{t - t_{end}/2}{1.5 \times 3600}\right)^2\right) \tag{14}$$

2.4 Time-Step Independence and Internal Energy-Balance Diagnostic

Table 1 (Section 3) summarizes the time-step check ($\Delta t = 0.2$ s vs. $\Delta t = 0.1$ s). The sunlit-window mean $\overline{\eta}_{solar}$ matches to six decimal places (0.878817 vs. 0.878816), while the RMS global energy-balance residual decreases from 0.086164 to 0.048758 J per step when refining Δt from 0.2 to 0.1 s. Grid independence note: the present model is spatially lumped (one temperature per control volume and one temperature per PCM layer). Therefore, "grid independence" is not applicable in the spatial sense; the only meaningful numerical resolution parameter is the temporal step size, which is explicitly verified in Table 1.

Table 1: Time-step check and energy-balance RMS (baseline parameter set; MATLAB diagnostic).

Case	Δt [s]	$\overline{\eta}_{solar}$ (–)	RMS Energy Residual [J·step−1]
Baseline (figures)	0.2	0.878817	0.086164
Refined	0.1	0.878816	0.048758

2.5 Validation Strategy (Transparent and Bounded)

Validation uses (A) literature-consistent benchmarking and (B) internal numerical diagnostics. Transient trends are compared against published PCM–ETSC studies [9–12] (trend-level, not point wise identity), and numerical consistency is documented via time-step refinement and the global energy-balance RMS residual [20].

2.6 Sensitivity Analysis Settings

One-at-a-time sensitivity varies (i) HTF mass flow rate $\dot{m}_f$ 0.01–0.04 kg s^{-1} in steps of 0.005 kg s^{-1}, (ii) a uniform PCM thickness over 0.015–0.05 m (five values), and (iii) a common melting-temperature shift ΔT_m over −5 to +15 K in steps of 5 K.

The bounds are chosen to remain in a practical ETSC–PCM operating class while avoiding near-stagnant conditions where a mixed-mean HTF temperature can drift toward the absorber temperature and make solar-referenced ratios overly sensitive to low-irradiance tails. The upper $\dot{m}_f$ bound corresponds to a high-flow regime used in the sweep and keeps convective extraction as the dominant useful pathway. The thickness range covers thin to relatively thick annular PCM layers that materially change thermal inertia and latent capacity without changing the governing structure of the lumped model. Finally, the melting-temperature shift range includes earlier activation (negative shift) and delayed activation (positive shift);

wider shifts were not pursued here because they produce many designs that never enter the mushy band within the 6 h horizon, which reduces interpretability of staged melting in a multilayer setting.

2.7 Multi-Objective Optimization (NSGA-II)

Multi-objective optimization maps the trade-off between the sunlit-window mean objectives ($\overline{\eta}_{solar}$ and $\overline{\Psi}_{solar}$) using NSGA-II (MATLAB gamultiobj) [19]. Decision variables are [$\dot{m}_f$, ΔT_m] with bounds $\dot{m}_f \in [0.01, 0.04]$ kg s^{-1} and $\Delta T_m \in [-5, 10]$ K. Solver settings are Population Size = 60, Max Generations = 30, rng (1) (random seed fixed for reproducibility), and parallel evaluation disabled.

3 Results

All simulations reported in this section use the transient model, boundary conditions, and KPI definitions introduced in Section 2. Unless otherwise noted, efficiencies are reported as solar-referenced quantities and are evaluated over the sunlit mask $G(t) > 0.1\, G_{max}$.

Figure numbering is: Fig. 2—temperatures; Fig. 3—liquid fractions; Fig. 4—thermal efficiency; Fig. 5—exergy efficiency; Figs. 6–8—one-at-a-time sensitivity sweeps; Fig. 9—Pareto front.

Figure formatting and readability. All figures are prepared with consistent proportions (i.e., no axis stretching), uniform font family and size across subplots, and consistent line widths and marker sizes. Export settings are selected for both print and on-screen viewing (vector PDF/EPS where possible; otherwise ≥600 dpi). Axis labels, legends, and tick marks are sized for single-column readability, and captions are aligned with the final figure filenames.

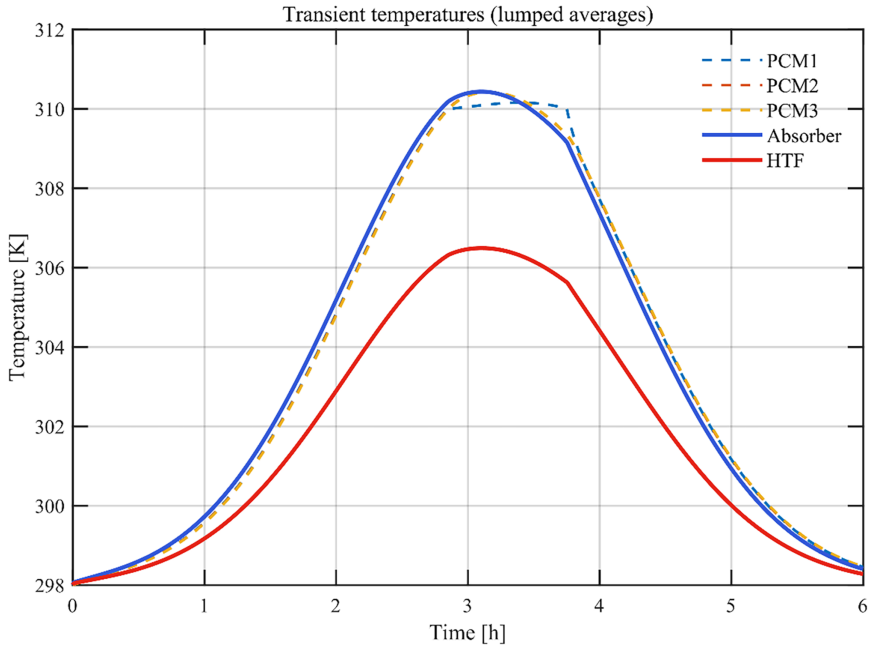

Figure 2: Transient lumped-mean temperatures of the absorber tube, the HTF, and the PCM layers under the baseline time-dependent irradiance profile.

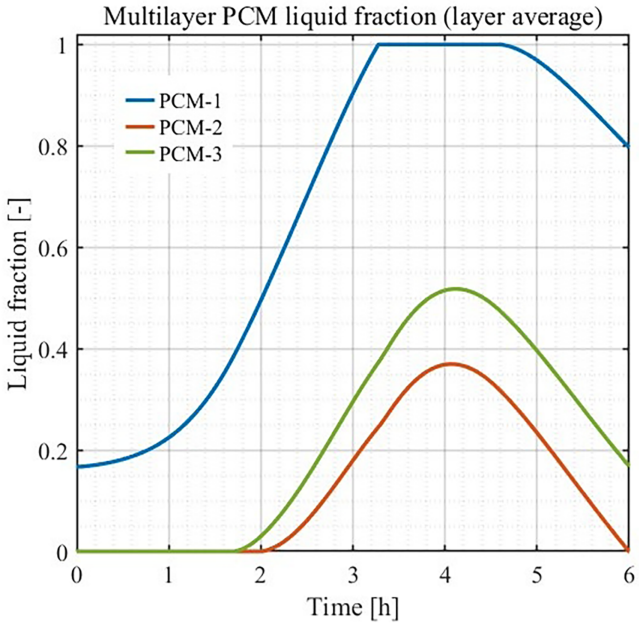

Figure 3: Multilayer PCM liquid fraction histories (layer averages) showing staged melting behavior.

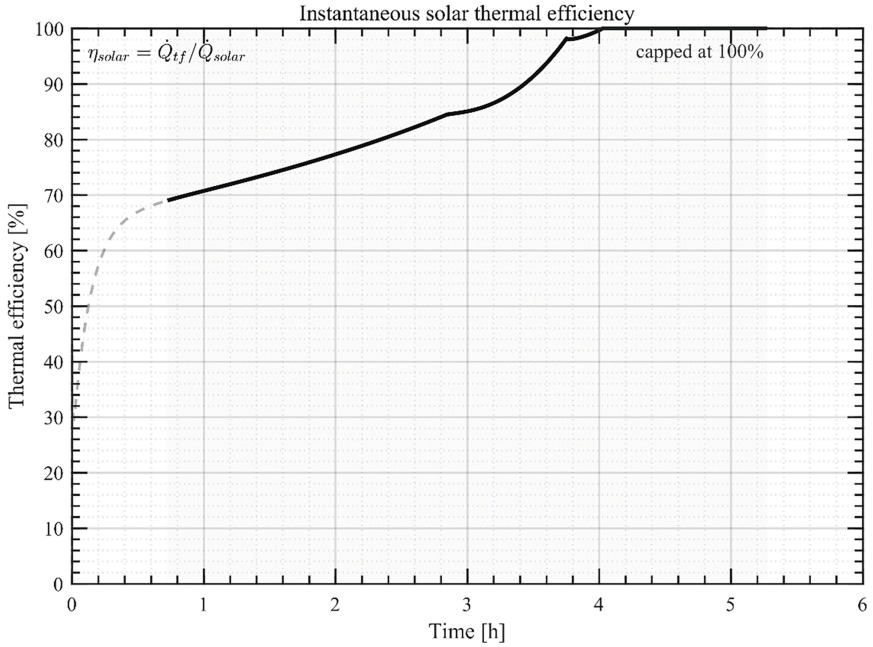

Figure 4: Instantaneous solar-referenced thermal efficiency, $\eta_{\mathrm{solar}}(t)$; the sunlit mask is applied when computing windowed mean values.

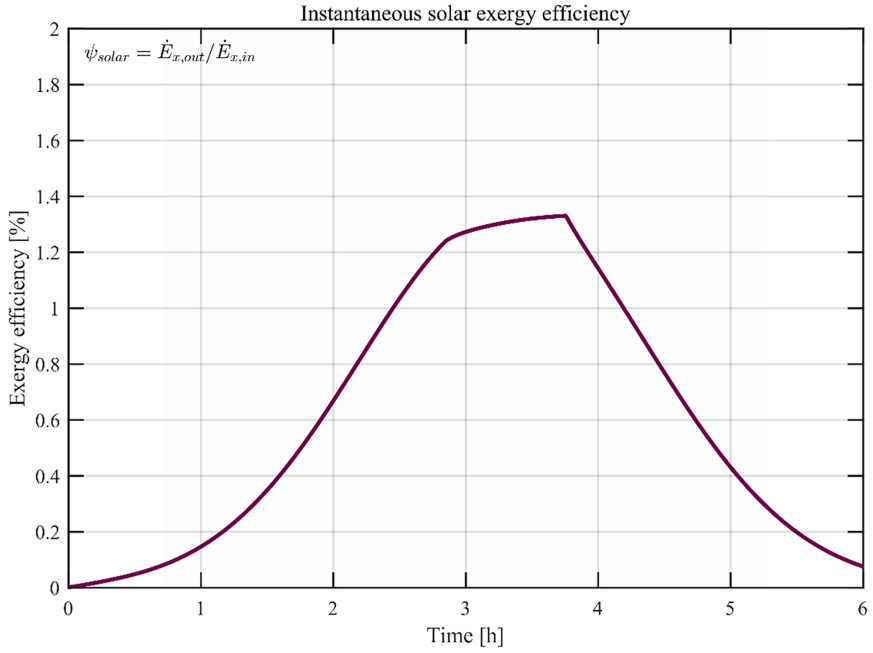

Figure 5: Instantaneous solar-referenced exergy efficiency, $\overline{\psi}_{solar}(t)$, computed using Petela-weighted solar exergy input and a bounded HTF exergy output.

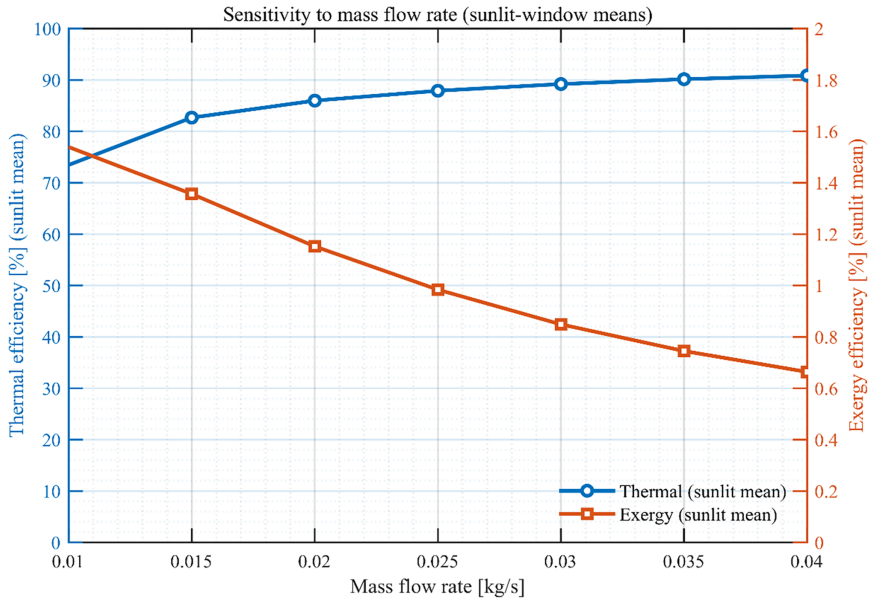

Figure 6: Sensitivity to HTF mass flow rate: sunlit-window mean thermal efficiency and sunlit-window mean exergy efficiency.

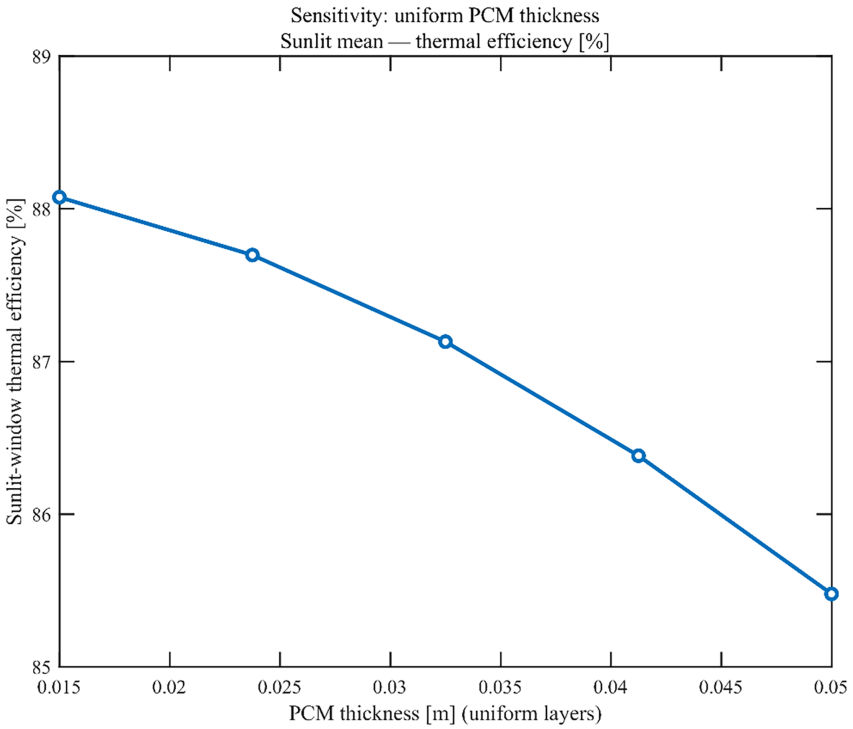

Figure 7: Sensitivity to uniform PCM thickness: sunlit-window mean thermal efficiency vs. L (uniform layers).

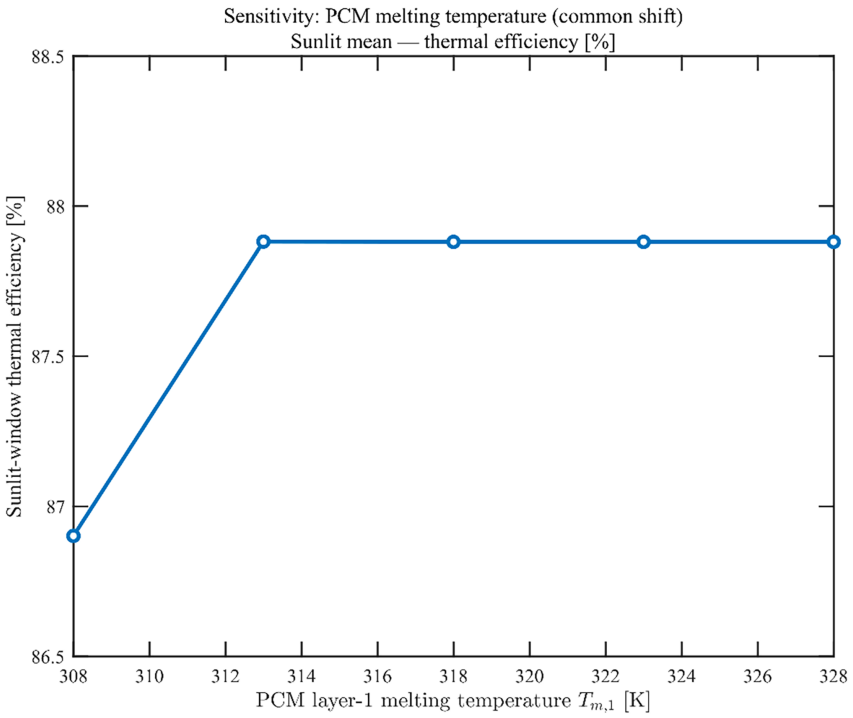

Figure 8: Sensitivity to PCM melting temperature: sunlit-window mean thermal efficiency vs. $T_{m,1}$ (after the applied shift).

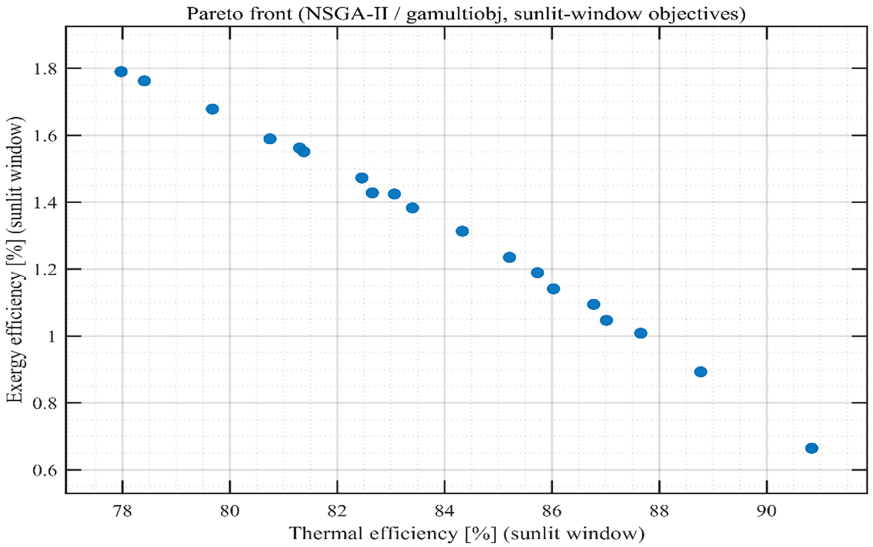

Figure 9: Pareto front (NSGA-II via MATLAB gamultiobj) for sunlit-window objectives ($\overline{\eta}_{solar}$, $\overline{\psi}_{solar}$).

3.1 Transient Temperatures and Comparison with the No-PCM Reference

Fig. 2 shows the lumped-mean temperatures of the absorber tube, the heat-transfer fluid, and each PCM layer. The no-PCM reference case is computed under the same G(t) and the same lumped absorber/HTF/radiation formulation, with the latent-storage pathway removed (NPCM = 0). For the numerical run used to generate the figures, the peak HTF temperature is 306.489 K with PCM and 306.774 K without PCM, while the peak absorber temperature is 310.432 K with PCM and 310.848 K without PCM. Compared with the no-PCM case, PCM integration reduces the peak HTF temperature by 0.284 K and the peak absorber temperature by 0.416 K.

3.2 Multilayer Melting Progression and Duration Metrics

Fig. 3 shows layer-averaged liquid fractions. Using $f_l \geq 0.99$ as a completion metric, none of the three layers reach completion within the 6 h horizon for the reported baseline, because peak layer temperatures remain below the upper mushy bound needed for near-complete melting given T_{mk} = (313, 318, 323) K and ΔT_{mushy} = 6 K.

3.3 Thermal Efficiency (Instantaneous) and Sunlit-Window Mean

Fig. 4 presents the instantaneous solar-referenced thermal efficiency, $\eta_{solar}(t)$, as defined in Section 2. Over the sunlit mask, $\overline{\eta}_{solar}$ = 0.8788 (87.88%).

3.4 Exergy Efficiency and Evolution

Fig. 5 presents the instantaneous solar-referenced exergy efficiency, $\psi_{solar}(t)$, as defined in Section 2. The simulation yields max ψ_{solar} = 0.0133. Over the sunlit window, the mean value is $\overline{\psi}_{solar}$ = 0.0098 (0.98%).

3.5 Numerical Resolution and Internal Energy-Balance Diagnostic

Table 1 summarizes the time-step refinement from Δt = 0.2 to 0.1 s. The sunlit-window mean $\overline{\eta}_{solar}$ is unchanged to six decimal places (0.878817 vs. 0.878816), while the RMS global energy-balance residual

decreases from 0.086164 to 0.048758 J per step, supporting the numerical consistency of the explicit time integration.

RMS energy residual [J·step−1] denotes the root-mean-square of the global energy-balance mismatch per time step (J per step).

3.6 Indirect Experimental Benchmarking (Literature Mapping)

Table 2 presents a quantitative, benchmarking-style comparison by compiling key indicators reported in the cited PCM–ETSC studies—such as peak temperature levels, efficiency metrics, and (where available) liquid-fraction completion behavior—and placing them alongside the corresponding indicators obtained from the present model. Because the tube layout, PCM arrangement, and KPI definitions differ across studies, the comparison is not pointwise replication; instead, it supports trend-level consistency in the direction and relative timing of PCM effects (charging buffering and melting evolution).

Table 2: Quantitative literature mapping (trend-level) for PCM–ETSC studies and corresponding present-model indicators.

Ref.	Source (Full Citation in References)	Outcome Reported in the Literature (as Stated in the Source)	Present Model Indicator (This Work)
[9]	Wu et al. (2022), Journal of Energy Storage	Field energy analysis of a PCM-integrated ETSC under measured irradiance; collector-side energy metrics are reported for the tested configuration.	Baseline with PCM: $T_f \in$ [298.000, 306.489] K and $T_t \in$ [298.000, 310.432] K; η_{solar} = 0.8788.
[10]	ALali et al. (2023), Diyala Journal of Engineering Sciences	Experimental U-pipe ETSC with and without PCM; melting/solidification times vary with flow rate, and PCM integration modifies temperature–time histories.	Peak reduction vs. no-PCM under identical G(t): $\Delta T_{f,max} = -0.284$ K and $\Delta T_{t,max} = -0.416$ K (Section 3.1).
[11]	Pathak et al. (2023), Sustainability	Energetic and exergetic efficiencies reported for a PCM-integrated ETSC; first-law and second-law trends do not necessarily coincide under transient windows.	η_{solar} = 0.8788; ψ_{solar} = 0.0098; max ψ_{solar} = 0.0133 (Sections 3.3 and 3.4).
[12]	Uniyal et al. (2023), Journal of Energy Storage	Melting evolution and heat-transfer behavior of PCM in a U-tube ETSC configuration, including liquid-fraction evolution vs. time.	Layer completion metric: no layer reaches $f_\ell \geq 0.99$ within 6 h for the reported baseline (Section 3.2).

3.7 One-at-a-Time Sensitivity Analysis

Figs. 6–8 report sunlit-window means vs. $\dot{m}_f$, uniform PCM thickness, and a common melting-temperature shift.

In the reported sweeps, the sunlit-window mean thermal efficiency increases with $\dot{m}_f$ (Fig. 6). Increasing uniform PCM thickness decreases the sunlit-window mean thermal efficiency (Fig. 6), reflecting the stronger thermal inertia and latent-capacity diversion in the lumped coupling framework.

For the PCM completion metric $f_l \geq 0.99$, none of the layers reaches completion within the 6 h horizon for the baseline case (Fig. 4). Therefore, in the explored thickness range, the thickness sensitivity in Fig. 7 is interpreted primarily through partial latent uptake and thermal-inertia effects, quantified by the sunlit-window efficiency endpoints reported in the figure (rather than a completion time that is undefined within the 6 h simulation horizon).

3.8 Multi-Objective Optimization and Representative Pareto Designs

Fig. 9 shows the non-dominated set obtained from NSGA-II for the sunlit-window objectives. The archived Pareto set contains 21 points spanning $\overline{\eta}_{solar}$ [0.780, 0.908] and $\overline{\psi}_{solar}$ [0.007, 0.018]. Representative designs reported from the same run are listed in Table 3.

Table 3: Representative Pareto points (same gamultiobj run as Fig. 9).

Case	$\dot{m}_f$ [kg·s^{-1}]	ΔTm [K]	$\overline{\eta}_{solar}$ (–)	$\overline{\psi}_{solar}$ (–)
A	0.03991	4.257	0.9084	0.0066
B	0.01055	9.382	0.7797	0.0179
C	0.01568	2.695	0.8340	0.0138

4 Discussion

4.1 Comparison with Prior PCM–ETSC and Multilayer PCM Studies

The simulated PCM–integrated case lowers peak HTF and absorber temperatures relative to the no-PCM reference under identical G(t) (Section 3.1). This directed change would then remained consistent with the experimental reporting on PCM–ETSC systems, whereby the latent buffering moderates the temperature excursions relative to a sensible only collectors, but the absolute temperature levels are still climate, load and loop configuration sensitive [9–12]. The multilayer temperature and phase-change traces also follows a staged progression consistent with the multilayer staging concepts [16].

4.2 Irreversibility Interpretation and the Exergy Response

The baseline run reaches max ψ_{solar} = 0.0133 while the sunlit mean remains $\overline{\psi}_{solar}$ = 0.0098, illustrating that instantaneous and windowed second-law indicators can diverge under transient charging.

A physically plausible explanation for this behaviour is that, quite early in the charging interval, the HTF temperature departs from the dead state (ambient) more rapidly than the collective absorber–PCM subsystem develops its higher-temperature response. There is thus a short period of time during which the extracted heat has a relatively favorable temperature potential. As the charging proceeds, the instantaneous useful extraction is increasingly dictated by both the heat transfer across finite temperature differences in the absorber, HTF, PCM layers, and the ongoing losses through radiative losses to the ambient. At the scale of the collector, these mechanisms begin contributing to irreversibility through (i) finite-ΔT heat transfer (absorber–HTF, absorber–PCM), (ii) the mixing of temperatures intrinsic to the mixed-mean HTF control-volume representation, and (iii) the heat rejection to the ambient (dead state) dealt with in terms of loss through radiative loss. Since ψ_{solar} is divided by Petela-weighted solar exergy input, transient shifts in the effective temperature level of the heat delivered are manifested early on as a peak, followed by decline in the window-averaged second-law metric.

4.3 Practical Design Guidance from Sensitivity and Pareto Results

These NSGA-II results provide thermal-oriented solutions (Case A), exergy-oriented (Case B), and compromise (Case C), thus allowing design selection in terms of the most preferred objective rather than a single "optimum".

Case A maximises η solar (i.e., all else being equal, the largest solar-referenced useful heat delivery over the sunlit window) at the expense of lower ψ_{solar}. Case B maximises $\overline{\psi}_{solar}$, i.e., the extracted heat is more second-law useful, under the particular exergy normalisation adopted here, at the expense of lower thermal efficiency. Case C sits between these two extremes in objective space, and represents a balanced operating point as both heat quantity and temperature potential is relevant to downstream use.

4.4 Limitations

For one, the validation here is indirect. We've anchored our transient trends against established PCM–ETSC experiments from the literature [9–12], rather than aiming for a perfect, point-by-point match with one specific lab setup or a single irradiance profile G(t). Second, the absorber, HTF, and each PCM layer are lumped; effective coefficients h_{tf} and h_{PCM} subsume three-dimensional and contact resistances. Third, the mushy region uses a fixed finite width ΔT_{mushy} = 6 K (Section 2), which regularizes the enthalpy method but should be reported alongside material uncertainty. Fourth, pump or auxiliary power is not subtracted in the reported efficiencies unless explicitly added in a future system model. Fifth, the Pareto search uses Δt = 1 s for speed while baseline figures use Δt = 0.2 s; objectives are therefore consistent with the optimization discretization and should not be reinterpreted as fine-grid limits without repeating the study at Δt = 0.2 s if reviewers require it. These limitations are consistent with transparency recommendations for modeling studies [20].

5 Conclusions

This study presented a transient enthalpy-based analysis of a multilayer PCM–assisted evacuated tube solar collector with time-dependent irradiance. Relative to a no-PCM reference, the PCM-integrated case reduces peak HTF temperature by 0.284 K and peak absorber temperature by 0.416 K for the baseline, demonstrating latent buffering of transient temperature excursions. Multilayer phase change is evidenced by staged liquid-fraction evolution (Fig. 2); however, under the baseline irradiance horizon and the adopted mushy-zone definition, none of the layers reaches the completion threshold $f_l \geq 0.99$ within 6 h. Sunlit-window means for the baseline are $\overline{\eta}_{solar}$ = 0.8788 and $\overline{\psi}_{solar}$ = 0.0098, while instantaneous ψ_{solar} reaches 0.0133, indicating divergence between first-law and second-law indicators during transient charging. Numerical consistency is supported by time-step refinement and reduced RMS energy residuals. Sensitivity and NSGA-II optimization map a clear thermal–exergy trade-off and provide representative Pareto designs for different priorities.

Acknowledgement: The authors thank Middle Technical University (MTU), Baghdad, for providing computing facilities used in this work.

Funding Statement: The authors received no specific funding for this study.

Author Contributions: Dheyaa Abdulraheem Khalaf: Conceptualization, Methodology, Software, Formal analysis, Investigation, Writing—original draft, Writing—review & editing. Ammar Sami Mohammad: Literature review, Validation support, Writing—review & editing. All authors reviewed and approved the final version of the manuscript.

Availability of Data and Materials: The MATLAB code and the simulation outputs supporting the findings of this study are available from the corresponding author upon reasonable request.

Ethics Approval: Not applicable.

Conflicts of Interest: The authors declare no conflicts of interest.

Nomenclature

Latin symbols		
Symbol	**Meaning**	**Unit**
Ac	Collector reference area	m^2
c_f	HTF specific heat	$J{\cdot}kg^{-1}{\cdot}K^{-1}$
c_t	Absorber specific heat	$J{\cdot}kg^{-1}{\cdot}K^{-1}$
$c_{p,k}$	PCM specific heat (layer (k))	$J{\cdot}kg^{-1}{\cdot}K^{-1}$
Ex	Exergy rate	W
f_l	Liquid fraction	–
G(t)	Irradiance	$W{\cdot}m^{-2}$
h_{tf}	Absorber–HTF coefficient	$W{\cdot}m^{-2}{\cdot}K^{-1}$
h_{pcm}	Absorber–PCM coefficient	$W{\cdot}m^{-2}{\cdot}K^{-1}$
L_k	PCM thickness (layer (k))	m
$L_{lat,k}$	Latent heat (layer (k))	$J{\cdot}kg^{-1}$
m_t	Absorber mass	kg
m_f	HTF CV mass	kg
$\dot{m}_f$	Mass flow rate	$kg{\cdot}s^{-1}$
N_{pcm}	Number of PCM layers	–
Q_{solar}	Absorbed solar power	W
$Q_{t\to f}$	Absorber→HTF heat rate	W
$Q_{t\to PCM}$	Absorber→PCM heat rate	W
Q_{loss}	Radiative loss	W
t	Time	s
T_{amb}	Ambient temperature	K
T_f	HTF temperature (mixed-mean)	K
T_t	Absorber temperature	K
$T_{pcm,k}$	PCM temperature (layer (k))	K
$T_{m,k}$	Melting temperature (layer (k))	K
T_{sun}	Sun temperature (Petela)	K
Greek symbols		
Symbol	**Meaning**	**Unit**
η_{opt}	Optical efficiency	–
η_{solar}	Solar-referenced thermal efficiency	–
ψ_{sun}	Petela factor	–
ψ_{solar}	Solar-referenced exergy efficiency	–
σ	Stefan–Boltzmann constant	$W{\cdot}m^{-2}{\cdot}K^{-4}$
Subscripts		
Subscript	**Meaning**	
amb	Ambient	
f	HTF	

(Continued)

(continued)

t	Absorber
Pcm	PCM
solar	Solar-referenced
k	PCM layer index

References

1. Kalogirou SA. Solar thermal collectors and applications. Prog Energy Combust Sci. 2004;30(3):231–95. doi:10.1016/j.pecs.2004.02.001.
2. IPCC Intergovernmental Panel on Climate Change. Climate change 2022—mitigation of climate change: working group III contribution to the sixth assessment report of the intergovernmental panel on climate change. Cambridge, UK: Cambridge University Press; 2023. doi:10.1017/9781009157926.
3. Sharma A, Tyagi VV, Chen CR, Buddhi D. Review on thermal energy storage with phase change materials and applications. Renew Sustain Energy Rev. 2009;13(2):318–45. doi:10.1016/j.rser.2007.10.005.
4. Zalba B, Marín JM, Cabeza LF, Mehling H. Review on thermal energy storage with phase change: materials, heat transfer analysis and applications. Appl Therm Eng. 2003;23(3):251–83. doi:10.1016/S1359-4311(02)00192-8.
5. Morrison GL. Solar water heating. In: Comprehensive renewable energy. Amsterdam, The Netherlands: Elsevier; 2012. p. 1–30.
6. Tian Y, Zhao CY. A review of solar collectors and thermal energy storage in solar thermal applications. Appl Energy. 2013;104:538–53. doi:10.1016/j.apenergy.2012.11.051.
7. Regin AF, Solanki SC, Saini JS. Heat transfer characteristics of thermal energy storage system using PCM capsules: a review. Renew Sustain Energy Rev. 2008;12(9):2438–58. doi:10.1016/j.rser.2007.06.009.
8. Farid MM, Khudhair AM, Razack SAK, Al-Hallaj S. A review on phase change energy storage: materials and engineering applications. Applied Energy. 2004;83(9):923–47. doi:10.1016/j.enconman.2003.09.015.
9. Wu Y, Tong X, Li D, Arıcı M, Liu C, Liu Y, et al. Energy analysis of evacuated tube solar collector integrating phase change material in Northeast China. J Energy Storage. 2022;55:105772. doi:10.1016/j.est.2022.105772.
10. ALali SN, Abdulateef J, Hassan Q, Jaszczur M. Thermal performance analysis of U-pipe evacuated tube solar heater system with and without PCM. Diyala J Eng Sci. 2023;34–48. doi:10.24237/djes.2023.160403.
11. Pathak SK, Tyagi VV, Chopra K, Pandey AK, Sari A, Abdulateef AM. Energetic, exergetic, and heat transfer assessment of PCM-integrated heat-pipe-based ETSC for clear and cloudy weather conditions. Sustainability. 2023;15(12):9780. doi:10.3390/su15129780.
12. Uniyal A, Prajapati YK, Suman S. Heat transfer and melting characteristics of the phase change material inside U-tube based evacuated tube solar collector. J Energy Storage. 2023;62:106918. doi:10.1016/j.est.2023.106918.
13. Harris I, James Rivas A, De Los Angeles Ortega Del Rosario M, Saghir MZ. Recent developments in phase change material-based solar water heating systems: insights on research trends and opportunities. Int J Thermofluids. 2023;20(7):100359. doi:10.1016/j.ijft.2023.100359.
14. Pathak SK, Tyagi VV, Chopra K, Pandey AK. Solar thermal potential of phase change material based U-pipe ETSCs for different climatic zones: evaluating energy matrices and economic viability. Sustain Mater Technol. 2024;40:e00857. doi:10.1016/j.susmat.2024.e00857.
15. Pathak S. Enhancement of solar evacuated tube unit filled with nanofluid and NEPCM. Scientific Reports. 2024;14(1):10952. doi:10.1038/s41598-024-58276-4.
16. Zayed ME, Zhao J, Elsheikh AH, Hammad FA, Ma L, Du Y, et al. Applications of cascaded phase change materials in solar water collector storage tanks: a review. Sol Energy Mater Sol Cells. 2019;199(2):24–49. doi:10.1016/j.solmat.2019.04.018.
17. Petela R. Exergy of undiluted thermal radiation. Sol Energy. 2003;74(6):469–88. doi:10.1016/S0038-092X(03)00226-3.

18. Voller VR, Prakash C. A fixed grid numerical modelling methodology for convection-diffusion mushy region phase-change problems. Int J Heat Mass Transf. 1987;30(8):1709–19. doi:10.1016/0017-9310(87)90317-6.
19. Deb K, Pratap A, Agarwal S, Meyarivan T. A fast and elitist multiobjective genetic algorithm: NSGA-II. IEEE Trans Evol Comput. 2002;6(2):182–97. doi:10.1109/4235.996017.
20. Coleman HW, Steele WG Jr. Experimentation, validation, and uncertainty analysis for engineers. 3rd ed. Hoboken, NJ, USA: John Wiley & Sons, Inc.; 2009. doi:10.1002/9780470485682.
21. Li Y, Liang X, Song W, Li T, Wang D, Liu Y. Optimization and thermal performance of U-type evacuated tube solar collector filled with phase change material. Energy Rep. 2022;8(2):6126–38. doi:10.1016/j.egyr.2022.04.054.
22. Ismail AO, Ayaal AH, Sulttan MQ. Thermal performance of the evacuated tube solar collector (ETSC) using (PCM) with different fluid flow rates. In: AIP Conference Proceedings. Baghdad, Iraq: AIP Publishing; 2024. p. 070026. doi:10.1063/5.0207652.
23. Said S, Mellouli S, Alqahtani T, Algarni S, Ajjel R, Alshammari BM, et al. Optimizing thermal performance of evacuated tube solar collectors with cascaded phase change materials. Case Stud Therm Eng. 2025;70(3):106138. doi:10.1016/j.csite.2025.106138.
24. Sathish T, Saravanan R, Giri J, Faisal RS, Alkhrissat T, Becheikh N, et al. Performance enhancement of evacuated tube solar collectors using Fe_3O_4Nanoparticle-enhanced phase change materials for efficient thermal energy storage. Eng Rep. 2025;7(7):e70230. doi:10.1002/eng2.70230.
25. Al-Abdali AM, Ammari H. Thermal energy storage using phase-change material in evacuated-tubes solar collector. AIMS Energy. 2022;10(3):486–505. doi:10.3934/energy.2022024.
26. Mourad A, Aissa A, Said Z, Younis O, Iqbal M, Alazzam A. Recent advances on the applications of phase change materials for solar collectors, practical limitations, and challenges: a critical review. J Energy Storage. 2022;49(1):104186. doi:10.1016/j.est.2022.104186.
27. Shoeibi S, Jamil F, Parsa SM, Mehdi S, Kargarsharifabad H, Ali Agha Mirjalily S, et al. Recent advancements in applications of encapsulated phase change materials for solar energy systems: a state of the art review. J Energy Storage. 2024;94(5):112401. doi:10.1016/j.est.2024.112401.
28. Aruna M, Nagabhooshanam N, Parihar PS, Kedia N, Jemmy Christy H, Satya G, et al. Enhancement of solar thermal performance and reduction of thermal loss behaviour of solar thermal collector featured with polyaniline and paraffin. Appl Therm Eng. 2025;278:127273. doi:10.1016/j.applthermaleng.2025.127273.
29. Mousavi SM, Sheikholeslami M. Enhancement of solar evacuated tube unit filled with nanofluid implementing three lobed storage unit equipped with fins. Sci Rep. 2024;14(1):7939. doi:10.1038/s41598-024-58276-4.
30. Said S, Mellouli S, Alqahtani T, Algarni S, Ajjel R, Alshammari BM, et al. Performance enhancement of evacuated U-tube solar collector integrated with phase change material. Case Stud Therm Eng. 2024;61:104948. doi:10.1016/j.csite.2024.104948.
31. Uniyal A, Prajapati YK, Kumar D. Experimental investigation of wire-mesh equipped U-tube evacuated tube collector integrated with phase change material for hot water generation. Appl Energy. 2025;377(134):124501. doi:10.1016/j.apenergy.2024.124501.
32. Wang X, Li D, Meng F, Wu Y, Yang R, Gao M, et al. Structure optimization of U-tube solar collector integrated with phase change materials. Appl Therm Eng. 2025;260(3):125052. doi:10.1016/j.applthermaleng.2024.125052.